Physics of Fluids

Instability and energy budget analysis of viscous coaxial jets under a radial thermal field

Ran Qiao (乔然), **Kai Mu** (穆恺), **Xisheng Luo** (罗喜胜), **and Ting Si** (司廷)

COLLECTIONS

Paper published as part of the special topic on Recent Advances in Theory, Simulations, and Experiments on Multiphase FlowsMPF2020

View Online   Export Citation   CrossMark

ARTICLES YOU MAY BE INTERESTED IN

Physics of Fluids GALLERY OF COVERS
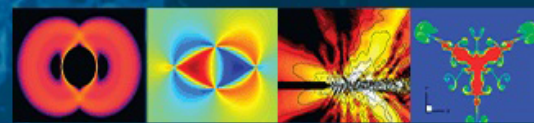
AIP Publishing

Instability and energy budget analysis of viscous coaxial jets under a radial thermal field

View Online   Export Citation   CrossMark

Ran Qiao (乔然), **Kai Mu (穆恺)**, **Xisheng Luo (罗喜胜)**, and **Ting Si (司廷)**[a]

AFFILIATIONS

Department of Modern Mechanics, University of Science and Technology of China, Hefei 230026, People's Republic of China

Note: This paper is part of the Special Topic, Recent Advances in Theory, Simulations, and Experiments on Multiphase Flows.
[a]Author to whom correspondence should be addressed: tsi@ustc.edu.cn

ABSTRACT

Temporal linear instability of viscous coaxial jets under a radial thermal field is carried out by considering axisymmetric and non-axisymmetric disturbances. The interfacial tensions of different fluids are taken to be temperature dependent. The para-sinuous, para-varicose, and helical unstable modes are identified in the Rayleigh regime. The energy budget is also employed to explore the relative importance of thermal-induced stresses on the jet instability at the most unstable wavenumber by changing the dimensionless parameters. It is shown that decreasing the temperature ratio of inner fluid to surrounding fluid (T_{13}) promotes the jet instability. For coaxial jets at $T_{13} > 1$, the Marangoni flow makes coaxial jets more stable, and increasing the fluid thermal conductivity suppresses the jet instability. For coaxial jets at $T_{13} < 1$, however, their influences on the jet instability are opposite. Compared with the thermal-induced stresses at the inner and outer interfaces, the inner interfacial tension is the main factor dominating the flow. Increasing either inner interfacial tension or outer surface tension and decreasing viscosity of any fluid can promote the instability of coaxial jets. The variations of thermal conductivity and specific heat capacity of either inner or surrounding fluids apparently influence the jet instability of the para-varicose mode, but hardly influence that of the para-sinuous mode. This work would provide great insight into the physical mechanism of thermal jet instability in various applications.

Published under license by AIP Publishing. https://doi.org/10.1063/5.0025880

I. INTRODUCTION

When two immiscible fluids are injected from a coaxial needle or injector into the surrounding medium, coaxial jets with double-interface structures can be formed. They are inherently unstable and will fragment into small drops because of flow instability. If the coaxial jets are heated or cooled, with different temperatures from the environment, additional Marangoni instability and thermal-capillary instability would have an impact on the breakup characteristics of coaxial jets.[1] This configuration exists widely in engineering industries such as inkjet printing,[1] preparation of metallic microdrops,[2] fiber spinning and coating,[3,4] and injection from rocket turbo.[5,6] Consequently, the understanding of the influences of the thermal field and thermophysical properties of fluids on the instability of coaxial jets is of great significance for various applications.

The instability behavior of coaxial jets has been studied intensively. Hertz and Hermanrud[7] formed coaxial liquid jets

experimentally by injecting fluids from the surface of a stationary liquid into air. They found three different types of flow modes and investigated the effects of physical properties on the jet instability. Sanz and Meseguer[8] established a one-dimensional model for the instability of inviscid coaxial jets and studied the influence of several parameters including the radius ratio, the density ratio, and the surface tension ratio, which were further compared with the experiments obtained by Hertz and Hermanrud.[7] Later, Meyer and Weihs[9] considered the influence of viscosity on the instability of coaxial jets. They studied the instability of a viscous annular jet moving in an inviscid inner and surrounding medium and carried out the parametric study including viscosity, velocity, and surface tension. Radev and Tchavdarov[10] took into account coaxial fluid jets with uniform velocity profile and ignored the ambient air, concluding that the surface tension was the dominant factor of the capillary instability. Shen and Li[11] considered coaxial jets with an inviscid inner gas and found two unstable modes, namely, the para-sinuous and para-various modes of coaxial jets. They concluded that there was a critical Weber

number, below which the jet instability was governed by the surface tension and above which the aerodynamic effect was the major source of the jet instability. Chauhan et al.[12] investigated the effects of annular fluid properties on jet breakup in temporal instability analysis and elucidated the conditions favoring compound droplet formation. Chen et al.[13] considered the viscous annular jets under either axisymmetric or non-axisymmetric disturbances and found that the axisymmetric mode was always the most unstable one. Ruo et al.[14] further studied non-axisymmetric disturbances of viscous coaxial jets with a uniform velocity profile moving in an inviscid surrounding gas. They found that the non-axisymmetric sinuous mode would dominate the flow at high Weber numbers and low Reynolds numbers. Segalini and Talamelli[15] discussed the effects of velocity profiles and Reynolds numbers on the jet breakup process. Afzaal et al.[16,17] examined the instability of a two-dimensional inviscid compound jet falling vertically downward in a surrounding gas under the influence of gravity. Ye et al.[18] considered the effect of viscoelasticity on the jet instability and found that the viscoelastic coaxial jets are more unstable than the Newtonian ones.

Previous studies have mainly focused on the breakup behavior of single jet when the thermal field exists. Chaudhury[19] focused on the heat transfer in a single liquid jet and developed an approximated heat flux equation to elucidate the initial development of the thermal boundary layer. Gill and Drazin[20] investigated the instability of compressible jets with long-wave disturbances and found that the long-wave disturbance was smaller in a hot jet than the corresponding isothermal case. Xu and Davis[21] examined an axial thermal field applied on liquid jet and found three unstable modes, called capillary, surface-wave, and thermal modes. Monkewitz and Sohn[22] analyzed the influences of velocity ratio, Mach number, and azimuthal wavenumber on the transition from absolute instability to convective instability. Dijkstra and Steen[23] considered a liquid bridge with an axial temperature gradient and found that thermocapillary-driven axial motions had a stabilization effect. Mashayek and Ashgriz[24] revealed convective behavior when the breakup occurred at the jet surface. They found that the thermocapillary effect would make jets more stable if thermal disturbances and surface disturbances were in-phase. Furlani[25] considered the influence of spatially varying surface tension in temporal instability and found that the breakup time of jets with thermal diffusion was relatively small because of the decay of the surface tension gradient.

In recent years, the instability of coaxial jets under a thermal field has drawn much attention due to its widely practical applications. For example, in a liquid rocket engine, there are hundreds of coaxial nozzle assemblies consisting of inner and outer channels that supply fuel and oxidant for injection, respectively. The initial temperatures of them before atomization are usually different. Perrault-Joncas and Maslowe[26] investigated the instability of an inviscid coaxial jet with a radial temperature gradient. The results indicated that an incompressible coaxial jet is more unstable than a compressible one. Mohanta et al.[27] considered a discontinuous temperature radial field and investigated the effect of heat and mass transfer on the instability of the confined jet in a tube. Mowlavi et al.[28] used both linear stability analysis and nonlinear simulations to investigate the physical mechanisms of the formation of silicon spheres by imposing a temperature field to a silicon-in-silica coaxial fiber. Jia et al.[29] examined confined coaxial jets under the gas

oscillations with heat and mass transfer. They found that mass and heat transfer suppressed the capillary instability. Li et al.[30] considered the temporal instability of a coaxial jet with only the outer fluid to be viscous and the outer surface tension to be temperature dependent. It can be found that as the thermal field is applied on coaxial jets, several thermal-induced effects would emerge, including the thermal-capillary effect, the Marangoni effect, and the heat transfer. However, previous studies on the breakup characteristics of thermal coaxial jets are still limited. It is desirable to explore the physical understanding of how they contribute to the jet instability, which motivates the present work.

We examine the temporal instability of viscous coaxial jets with axisymmetric and non-axisymmetric disturbances under a radial thermal field in this work. Consequently, we carry on the energy budget to gain insight into the physical mechanism of thermal influences on the jet instability. Additionally, the effects of thermophysical properties on the jet instability are analyzed. This paper is structured as follows: The physical model, the governing equations, the basic state of flow and temperature profiles, and the energy budget are constructed in Sec. II. The results and discussion are presented in Sec. III by considering a group of various dimensionless parameters. The conclusions are finally drawn in Sec. IV.

II. FORMULATION OF THE PROBLEM

A. Physical model and dimensionless parameters

A coaxial jet surrounded by the unbounded stationary air is considered in the cylindrical coordinate (z, r, θ), as sketched in Fig. 1. The thermal field perpendicular to the symmetric axis is imposed. The radii of inner and outer fluids are R_1 and R_2, respectively. Fluids in three subdomains are different in density ρ_i, viscosity μ_i, flow velocity $\mathbf{u}_i$, specific heat capacity C_{pi}, thermal conductivity k_i, and temperature T_i, where the subscripts $i = 1, 2, 3$ stand for the inner, outer, and surrounding phases, respectively. These three fluids form the inner and outer interfaces, and the inner and outer interfacial tensions are defined as $\sigma_i = \sigma_{i0} - \gamma_i(T - T_{30})$, where $\gamma_i = -d\sigma_i/dT > 0$ is the temperature-dependent coefficient of the interfacial tension (the subscripts $i = 1, 2$ stand for the inner or outer interfaces) and T_{30} is the temperature of the surrounding fluid in basic state. There are several assumptions reasonably given in our physical model: (i) All fluids are assumed to be incompressible viscous Newtonian fluids. (ii) The effect of gravity is neglected. (iii) There is no mass transfer through each interface.

The characteristic scales in this work are the length R_2, the velocity $\bar{U}_2$ (the average velocity of the outer annulus jet in basic
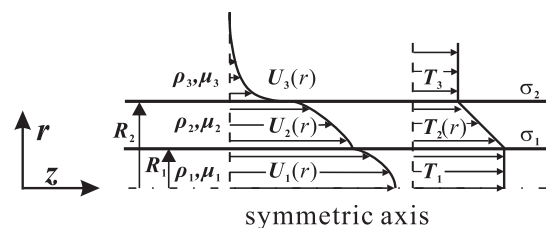

FIG. 1. Sketch of the coaxial jet model under a radial thermal field.

flow), the temperature T_{30}, the pressure $\rho_2 \bar{U}_2^2$, the density ρ_2, the viscosity μ_2, the interfacial tension σ_{20}, the temperature-dependent coefficient of interface tension γ_2, the thermal conductivity k_2, and the specific heat capacity C_{p2}. There are two characteristic times for the coaxial jets under a thermal field: the thermal conductive time $\tau_d = R_2^2 \rho_2 C_{p2}/k_2$ and the convective flow time $\tau_c = R_2/\bar{U}_2$. The ratio between them, known as the Péclet number ($Pe = \rho_2 C_{p2} \bar{U}_2 R_2/k_2$), shows the relative importance between the convection effect and the heat transfer. The Marangoni number ($Ma = \gamma_2 T_{30} R_2 \rho_2 C_{p2}/\mu_2 k_2$) shows the relevant importance of the thermal stress on the outer surface to the viscous stress of outer fluid. Some other dimensionless parameters involved in this problem are the Weber number $We = \rho_2 \bar{U}_2^2 R_2/\sigma_{20}$ and the Reynolds number $Re = \rho_2 \bar{U}_2 R_2/\mu_2$. There are several ratios about structure parameters and physical properties: the ratio of radius $\kappa_1 = R_1/R_2$, the ratio of temperature $T_{13} = T_{10}/T_{30}$, the ratios of density $\rho_{12} = \rho_1/\rho_2$ and $\rho_{32} = \rho_3/\rho_2$, the ratios of viscosity $\mu_{12} = \mu_1/\mu_2$ and $\mu_{32} = \mu_3/\mu_2$, the ratios of specific heat capacity $C_{p12} = C_{p1}/C_{p2}$ and $C_{p32} = C_{p3}/C_{p2}$, the ratios of thermal conductivity $k_{12} = k_1/k_2$ and $k_{32} = k_3/k_2$, the ratio of surface tension $\sigma_{12} = \sigma_{10}/\sigma_{20}$, and the ratio of temperature-dependent coefficient of interface tension $\gamma_{12} = \gamma_1/\gamma_2$.

B. Linear stability analysis

In linear stability theory, the flow variables are composed into the basic flow quantities and infinitesimal disturbances,

$$(u_i, v_i, w_i, p_i, T_i) = (U_i, 0, 0, P_i, T_{i0}) + (\tilde{u}_i, \tilde{v}_i, \tilde{w}_i, \tilde{p}_i, \tilde{T}_i). \quad (1)$$

Keeping the leading order of the disturbance equations, we obtain the linear governing equations and corresponding boundary conditions. The dimensionless linear continuity, momentum, and energy equations are

$$\nabla \cdot \tilde{\boldsymbol{u}}_i = 0, \quad (2)$$

$$\frac{\partial \tilde{\boldsymbol{u}}_i}{\partial t} + \tilde{\boldsymbol{u}}_i \cdot \nabla \boldsymbol{U}_i + \boldsymbol{U}_i \cdot \nabla \tilde{\boldsymbol{u}}_i = -\nabla \tilde{p}_i + \frac{1}{Re_i} \nabla^2 \tilde{\boldsymbol{u}}_i, \quad (3)$$

$$\frac{\partial \tilde{T}_i}{\partial t} + \tilde{\boldsymbol{u}}_i \cdot \nabla T_i + \boldsymbol{U}_i \cdot \nabla \tilde{T}_i = \frac{1}{Pe_i} \nabla^2 \tilde{T}_i, \quad (4)$$

where subscript $i = 1, 2, 3$, $Re_1 = Re \cdot \rho_{12}/\mu_{12}$, $Re_2 = Re$, $Re_3 = Re \cdot \rho_{32}/\mu_{32}$, $Pe_1 = Pe \cdot \rho_{12} C_{p12}/k_{12}$, $Pe_2 = Pe$, and $Pe_3 = Pe \cdot \rho_{32} C_{p32}/k_{32}$. Note that the viscosity dissipation is ignored here because of its tiny influence on the heat transfer compared with the heat conduction term.

Three components of the velocity, pressure, and temperature at the symmetry axis $r = 0$ satisfy the consistency conditions,

$$\tilde{v}_1 = \tilde{w}_1 = \frac{\partial \tilde{u}_1}{\partial r} = \frac{\partial \tilde{p}_1}{\partial r} = \frac{\partial \tilde{T}_1}{\partial r} = 0(n = 0), \quad (5)$$

$$\tilde{u}_1 = \tilde{p}_1 = \tilde{T}_1 = 0, \tilde{v}_1 + \frac{\partial \tilde{w}_1}{\partial \theta} = 0, 2\frac{\partial \tilde{v}_1}{\partial r} + \frac{\partial^2 \tilde{w}_1}{\partial r \partial \theta} = 0(n = 1), \quad (6)$$

$$\tilde{u}_1 = \tilde{v}_1 = \tilde{w}_1 = \tilde{p}_1 = \tilde{T}_1 = 0(n \geq 2), \quad (7)$$

where n stands for the azimuthal wavenumber, which is a non-negative integer. Previous numerical study shows that the

Marangoni flow will benefit the helical mode,[31] but its effect on coaxial jets has not been investigated by the theoretical analysis yet.

At the inner and outer interfaces, the kinematic boundary condition, the continuity of the velocity, temperature disturbances, and the corresponding heat flux should be satisfied, so as to balance the tangential and normal stresses.

Along the inner interface $r = \kappa_1 + \tilde{\eta}_1$,

$$\tilde{v}_1 = \left(\frac{\partial}{\partial t} + U_1 \frac{\partial}{\partial z}\right)\tilde{\eta}_1, \quad (8)$$

$$\tilde{u}_1 + \frac{dU_1}{dr}\tilde{\eta}_1 = \tilde{u}_2 + \frac{dU_2}{dr}\tilde{\eta}_1, \quad (9)$$

$$\tilde{v}_1 = \tilde{v}_2, \tilde{w}_1 = \tilde{w}_2, \tilde{T}_1 = \tilde{T}_2, \quad (10)$$

$$k_{12}\frac{\partial \tilde{T}_1}{\partial r} = \frac{\partial \tilde{T}_2}{\partial r}. \quad (11)$$

Along the outer interface $r = 1 + \tilde{\eta}_2$,

$$\tilde{v}_2 = \left(\frac{\partial}{\partial t} + U_2 \frac{\partial}{\partial z}\right)\tilde{\eta}_2, \quad (12)$$

$$\tilde{u}_2 + \frac{dU_2}{dr}\tilde{\eta}_2 = \tilde{u}_3 + \frac{dU_3}{dr}\tilde{\eta}_2, \quad (13)$$

$$\tilde{v}_2 = \tilde{v}_3, \tilde{w}_2 = \tilde{w}_3, \tilde{T}_2 = \tilde{T}_3, \quad (14)$$

$$\frac{\partial \tilde{T}_2}{\partial r} = k_{32}\frac{\partial \tilde{T}_3}{\partial r}. \quad (15)$$

Equilibriums of the normal stress at the inner and outer interfaces are

$$\tilde{p}_1 - \tilde{p}_2 - \mu_{12}\frac{2}{Re}\frac{\partial \tilde{v}_1}{\partial r} + \frac{2}{Re}\frac{\partial \tilde{v}_2}{\partial r}$$
$$= \frac{\sigma_{12}}{We}\left(\frac{\partial^2}{\partial z^2} + \frac{1}{\kappa_1^2}\right)\tilde{\eta}_1 - \frac{Ma}{PeRe}(T_{13} - 1)\left(\frac{\partial^2}{\partial z^2} + \frac{1}{\kappa_1^2}\right)\tilde{\eta}_1$$
$$- \frac{\gamma_{12}Ma}{PeRe}\frac{\tilde{T}_1}{\kappa_1}, \quad (16)$$

$$\tilde{p}_2 - \tilde{p}_3 - \frac{2}{Re}\frac{\partial \tilde{v}_2}{\partial r} + \mu_{32}\frac{2}{Re}\frac{\partial \tilde{v}_3}{\partial r} = \frac{1}{We}\left(\frac{\partial^2}{\partial z^2} + 1\right)\tilde{\eta}_2 - \frac{Ma}{PeRe}\tilde{T}_3. \quad (17)$$

Equilibriums of the tangential stress at inner and outer interfaces are

$$\left(\frac{d^2 U_2}{dr^2}\tilde{\eta}_1 + \frac{\partial \tilde{u}_2}{\partial r} + \frac{\partial \tilde{v}_2}{\partial z}\right) - \mu_{12}\left(\frac{d^2 U_1}{dr^2}\tilde{\eta}_1 + \frac{\partial \tilde{u}_1}{\partial r} + \frac{\partial \tilde{v}_1}{\partial z}\right)$$
$$= -\gamma_{12}\frac{Ma}{Pe}\frac{\partial \tilde{T}_1}{\partial z}, \quad (18)$$

$$\mu_{32}\left(\frac{d^2 U_3}{dr^2}\tilde{\eta}_2 + \frac{\partial \tilde{u}_3}{\partial r} + \frac{\partial \tilde{v}_3}{\partial z}\right) - \left(\frac{d^2 U_2}{dr^2}\tilde{\eta}_2 + \frac{\partial \tilde{u}_2}{\partial r} + \frac{\partial \tilde{v}_2}{\partial z}\right)$$
$$= -\frac{Ma}{Pe}\frac{\partial \tilde{T}_3}{\partial z}. \quad (19)$$

Equilibriums of the azimuthal stress at inner and outer interfaces are

$$\left[\frac{\partial \tilde{w}_2}{\partial r} + \frac{1}{\kappa_1}\left(\frac{\partial \tilde{v}_2}{\partial \theta} - \tilde{w}_2\right)\right] - \mu_{12}\left[\frac{\partial \tilde{w}_1}{\partial r} + \frac{1}{\kappa_1}\left(\frac{\partial \tilde{v}_1}{\partial \theta} - \tilde{w}_1\right)\right]$$
$$= -\gamma_{12}\frac{Ma}{Pe}\frac{\partial \tilde{T}_1}{\partial \theta}, \tag{20}$$

$$\mu_{32}\left[\frac{\partial \tilde{w}_3}{\partial r} + \left(\frac{\partial \tilde{v}_3}{\partial \theta} - \tilde{w}_3\right)\right] - \left[\frac{\partial \tilde{w}_2}{\partial r} + \left(\frac{\partial \tilde{v}_2}{\partial \theta} - \tilde{w}_2\right)\right] = -\frac{Ma}{Pe}\frac{\partial \tilde{T}_3}{\partial \theta}. \tag{21}$$

The far-field conditions are

$$\tilde{u}_3 = \tilde{v}_3 = \tilde{w}_3 = \tilde{p}_3 = \tilde{T}_3 = 0. \tag{22}$$

The normal mode method is employed to examine the stability of the basic flow with wavelike perturbations. The perturbations of the axial, radial, and azimuthal velocity $\tilde{u}_i$, $\tilde{v}_i$, and $\tilde{w}_i$, respectively, the pressure $\tilde{p}_i$, the temperature $\tilde{T}_i$, and the displacement of inner and outer interfaces are all decomposed into the Fourier exponential, i.e.,

$$(\tilde{u}_i, \tilde{v}_i, \tilde{w}_i, \tilde{p}_i, \tilde{T}_i) = (\hat{u}_i(r), \hat{v}_i(r), \hat{w}_i(r), \hat{p}_i(r), \hat{T}_i(r))e^{i(\alpha z+n\theta)+\beta t}, \tag{23}$$

$$(\tilde{\eta}_1, \tilde{\eta}_2) = (\hat{\eta}_1, \hat{\eta}_2)e^{i(\alpha z+n\theta)+\beta t}, \tag{24}$$

where α is the dimensionless real axial wavenumber and $\beta = \beta_r + i\beta_i$ is the dimensionless complex frequency. Note that the β_r stands for the temporal growth rate, and the β_i means the oscillation frequency.

In this work, the Chebyshev spectral collocation method is employed to solve the governing equations and boundary conditions we got above. First, we need to map the radial coordinate r into the calculation space $y \in [-1, 1]$. For the inner fluid $r \in [0, \kappa_1]$, the transform is

$$r = \frac{\kappa_1(1+y)}{2}; \tag{25}$$

for the outer liquid $r \in [\kappa_1, 1]$, it is

$$r = \frac{(\kappa_1 - 1)y + (\kappa_1 + 1)}{2}. \tag{26}$$

The transform of the surrounding air is

$$r = \frac{(\kappa_2 - 1)y + (\kappa_2 + 1)}{2}, \tag{27}$$

where $\kappa_2 = R_3/R_2$ means the outer limit of the computational domain. Second, we need expand characteristic functions $\hat{u}_i$, $\hat{v}_i$, $\hat{w}_i$, $\hat{p}_i$, and $\hat{T}_i$ into the Chebyshev polynomial form. Then, we put them and their derivatives into governing equations and boundary conditions and obtain discrete equations. Assuming that collocations of the inner, outer, and surrounding domains are $N_1 + 1$, $N_2 + 1$, and $N_3 + 1$ respectively, we obtain the computational matrix formed as $\boldsymbol{AX} = \beta \boldsymbol{BX}$, where $\boldsymbol{X}$ means the characteristic vector. Note that the size of two coefficient matrices $\boldsymbol{B}$, $\boldsymbol{A}$ is $(5N_1 + 5N_2 + 5N_3 + 17)$ $\times (5N_1 + 5N_2 + 5N_3 + 17)$.

C. Basic velocity and thermal profiles

In the cylindrical coordinate system (z, r, θ), the components of the basic velocity are

$$\boldsymbol{U}_i = (U_i, V_i, W_i) = (U_i(r), 0, 0), i = 1, 2, 3. \tag{28}$$

For the inner and outer fluids, the dimensionless momentum equations can be reduced as

$$\frac{1}{r}\frac{d}{dr}\left[r\frac{dU_1(r)}{dr}\right] = -\frac{G_1}{\mu_{12}Re}, \tag{29}$$

$$\frac{1}{r}\frac{d}{dr}\left[r\frac{dU_2(r)}{dr}\right] = -\frac{G_2}{Re}, \tag{30}$$

where $G_i = -\partial p_i/\partial z$ stands for the adverse pressure gradient. According to the normal stress equilibrium at the inner interface, we set $G_1 = G_2 = G$. As a consequence, we obtain a general solution

$$U_1(r) = -\frac{G}{4\mu_{12}Re}r^2 + B_1\ln(r) + C_1, \tag{31}$$

$$U_2(r) = -\frac{G}{4Re}r^2 + B_2\ln(r) + C_2, \tag{32}$$

with the constants B_i and C_i to be solved. Considering the boundary conditions such as the limitation at the axis, the tangential stress equilibrium, and the continuity of the velocity, we can obtain the velocity profile as

$$U_1(r) = \bar{U}_1 + \frac{1 - \bar{U}_1}{\kappa_1^2 + \mu_{12}(1 - \kappa_1^2)}\left(2r^2 - \kappa_1^2\right), \tag{33}$$

$$U_2(r) = 1 + \frac{\mu_{12}(1 - \bar{U}_1)}{\kappa_1^2 + \mu_{12}(1 - \kappa_1^2)}\left[2r^2 - (\kappa_1^2 + 1)\right], \tag{34}$$

where $\bar{U}_1$ means the dimensionless average velocity of the inner fluid jet.

It is difficult to obtain the analytical solution of the velocity profile of the surrounding gas by solving governing equations and boundary conditions directly. However, it has been successful to use the approximate velocity profile in theoretical analysis compared with the experimental results.[32,33] Here, we employ the co-error function to model the velocity decay in the boundary layer. The continuous condition, the balance of the tangential stress condition at the outer interface, and the no-perturbation condition far from the outer interface should be satisfied. Then, we obtain

$$U_3(r) = c \cdot \text{erfc}\left[\frac{2\sqrt{\pi}\mu_{12}(1 - \bar{U}_1)(1 - r)}{\mu_{32}\left[1 + \mu_{12}b(1 - \kappa_1^2)\right]\left[\mu_{12} + (1 - \mu_{12})\kappa_1^2\right]}\right], \tag{35}$$

with $b = (1 - \bar{U}_1)/\left[\mu_{12} + (1 - \mu_{12})\kappa_1^2\right]$ and $c = 1 + \mu_{12}b(1 - \kappa_1^2)$.

Similarly, as the thermal fields in practical applications are too complicated to formulate directly, a piecewise temperature profile is employed in the simplified physical model. The temperatures of the inner fluid and surrounding fluid are assumed to remain constant, and the temperature of outer fluid has a linear variation along the radial direction. Because we choose T_{30} as the characteristic temperature, which means the initial state at the surrounding environment, the dimensionless thermal field follows

$$T_1 = T_{13}, T_3 = 1, \tag{36}$$

$$T_2(r) = T_{13} + \beta_T(r - \kappa_1), \tag{37}$$

where $\beta_T = (1 - T_{13})/(1 - \kappa_1)$ shows the temperature gradient between the inner fluid and surrounding environment.

It should be mentioned that the velocity and temperature profiles are not able to strictly satisfy the governing equations and boundary conditions. However, in order to simplify the mathematical procedure and preserve the main characteristics of the flow, the basic states of velocities and temperatures should be given in a simplified way when investigating the instability characteristic of jets. For example, the error function[32,33] and the hyperbolic tangent function[5,26] can be utilized to simplify the practical velocity profiles. Moreover, several temperature profiles with the corresponding heat flux being discontinuous at the interface are also used as the approximate models,[21,27,29] which achieved the success in predicting the influence of thermal fields on the jet instability. In this work, the Péclet number is quite high in the reference state (i.e., $Pe = 500$), so the flow motion develops more quickly than the heat transfer. It is acceptable to adopt such piecewise temperature profiles in the locally linear instability analysis.

D. Energy budget analysis

The energy budget is an elaborate method in tracing the resource of the jet instability.[34–36] First, we consider a control volume whose length equals the wavelength of disturbance. Forming a dot product of dimensionless momentum equations (3) with dimensionless disturbance velocity $\tilde{u}_i$, integrating over the control volume V and a period $T = 2\pi/\beta_i$, and averaging over one wavelength λ and one period, one can obtain the equation about the development of kinetic energy. We use continuity equation to simplify it and use Gauss theorem to transfer certain volume integrals to surface integrals, and then, we derive the energy equation,

$$\frac{1}{T\lambda}\int_0^T\int_V\left(\frac{\partial}{\partial t} + \boldsymbol{U}_i \cdot \nabla\right)e\,dV\,dt$$
$$= -\frac{1}{T\lambda}\int_0^T\int_V \tilde{\boldsymbol{u}}_i \cdot [\tilde{\boldsymbol{u}}_i \cdot \nabla \boldsymbol{U}_i]\,dV\,dt - \frac{1}{T\lambda}\int_0^T\int_A p_i\tilde{\boldsymbol{u}}_i \cdot \boldsymbol{n}_i\,dA\,dt$$
$$+ \frac{1}{T\lambda Re_i}\int_0^T\int_A (\tilde{\boldsymbol{u}}_i \cdot \boldsymbol{\tau}_i) \cdot \boldsymbol{n}_i\,dA\,dt$$
$$- \frac{1}{2T\lambda Re_i}\int_0^T\int_V \boldsymbol{\tau}_i \cdot \boldsymbol{\tau}_i\,dV\,dt, \tag{38}$$

where $e = \tilde{\boldsymbol{u}}_i \cdot \tilde{\boldsymbol{u}}_i/2$ is the disturbance kinetic energy. $\boldsymbol{\tau}_i = \nabla\tilde{\boldsymbol{u}}_i + (\nabla\tilde{\boldsymbol{u}}_i)^T$ is the strain rate tensor where the superscript T stands for the transposition. A stands for the surface of the control volume. The subscript $i = 1, 2$ means the inner and outer fluids, respectively. Thus, the term on the left-hand side represents the rate of change of the disturbance kinetic energy. The first term on the right-hand side gives the work done by energy transfer between the disturbance and the basic flow. The second and third parts on the right-hand side represent the work done by the pressure and the viscous stress of the fluid. The last term gives the viscous energy dissipation. We employ both normal and tangential dynamic boundary conditions to transform the second and third integrals on the right-hand side in order

to better explain the effect of interface motion. Then, we can derive the energy budget as

$$KE_1 = REY_1 + PRL_{1S} + NVL_{1S} + SUT_1 + SUT_{1T} + PRL_{1R}$$
$$+ SHL_{1R} + NVL_{1R} + SHB_1 + SHL_{1S} + DIS_1$$
$$+ INS + ITS,$$
$$KE_2 = REY_2 + PRG_2 + NVG_2 + SUT_2 + PRL_{2S} + PRL_{2R}$$
$$+ SHB_2 + SHG_2 + SHL_{2S} + NVL_2 + SHL_{2R} + DIS_2$$
$$+ ONS + OTS. \tag{39}$$

The detailed formula of each term can be found in Appendixes A and B. The subscripts R and S stand for the transverse and side surface integrals of the control volume, respectively. KE_1 and KE_2 stand for the time rate of the kinetic energy of the inner fluid and outer fluid, respectively. REY_1 and REY_2 show the energy exchange between basic flow and disturbance velocities through the Reynolds stress of the inner fluid and outer fluid. DIS_1 and DIS_2 represent the rate of work done by the viscous dissipation. PRL_{1R} and PRL_{1S} are the rates of work done by the pressure fluctuation on the horizontal and side parts of the inner fluid control volume, respectively, so as to become PRL_{2R} and PRL_{2S}, which react to the outer fluid control volume. SHL_{1R} and SHL_{1S} stand for the work done by normal components of viscous stress at horizontal and side sections of the inner fluid, while SHL_{2R} and SHL_{2S} are those of the outer fluid. NVL_{1R} and NVL_{1S} stand for the rates of work done by the tangential components of viscous stress at horizontal and side sections of the inner fluid, respectively. SUT_1 and SUT_2 are the rates of work done by the inner interfacial tension and outer surface tension, respectively. SHB_1 and SHB_2 represent the rates of work done by the distortion of basic flow associated with the inner interfacial and outer surface displacements, respectively. PRG_2 shows the rate of work done by the interaction with outer liquid and surrounding gas. NVG_2 and SHG_2 are the rates of work done by the normal and shear viscous stress by the fluctuating ambient gas. NVL_2 shows the rate of work done by the tangential part of viscous stress at the outer side section of the control volume. These are five terms directly related to the thermal field. SUT_{1T} shows the rate of work done by the difference between interfacial tension changing with T_{13} and referenced value whose $T_{13} = 1$. It illustrates the influence of the temperature ratio on the capillary instability of the inner interface by changing the inner interfacial tension. INS is related to the periodic temperature perturbation at the inner interface. Therefore, it shows the rate of work done by the thermal-capillary stress on the inner interface. ITS means the rate of work done by the Marangoni stress on the inner interface. Similarly, ONS and OTS stand for the rates of work done by the thermal-capillary stress and Marangoni stress on the outer surface, respectively. Then, we normalize these terms by the kinetic energy of the entire system.[18,37] Because of the independence of each integrals, we can compare the KE_i with the sum of all terms on the right-hand side to guarantee the calculation accuracy.

III. RESULTS AND DISCUSSION

During the actual calculation, the dimensionless radius κ_2 of the surrounding fluid domain should be finite and constant. To guarantee the convergence of the code and meet the desired accuracy, we

TABLE I. Convergence of the complex growth rate for different numbers of collocation points and the surrounding fluid domain.

| κ_2	N_1	N_2	N_3	β_r	β_i
7	20	20	60	0.406 519	−1.127 610
6	20	20	60	0.406 461	−1.138 185
8	20	20	60	0.406 515	−1.127 597
7	10	20	60	0.406 519	−1.127 610
7	30	20	60	0.406 520	−1.127 610
7	20	10	60	0.406 502	−1.127 605
7	20	30	60	0.406 519	−1.127 610
7	20	20	50	0.406 518	−1.127 610
7	20	20	70	0.406 520	−1.127 610

set the value of $\kappa_2 = 7$ and choose the numbers of the collocation points to be $N_1 = 20$, $N_2 = 20$, and $N_3 = 60$ for the inner liquid, outer liquid, and surrounding gas subdomains, respectively. As shown in Table I, the convergence is guaranteed, and at least, three digits are satisfied.

To check the validity of our code, we ignore the density and viscosity of surrounding gas ($\rho_3 = 0$, $\mu_3 = 0$) and assume that there is no flow under the base state [$U_1(r) = U_2(r) = U_3(r) = 0$], which is exactly the same as the case studied by Chauhan *et al.*[12] previously. The dimensionless parameters are chosen as follows:

$$n = 0, \ \rho_{12} = 1, \ \mu_{12} = 1, \ \kappa_1 = 0.5,$$

$$\sigma_{12} = 0.5, \ We = 1, \ Re = 63.25.$$

The results obtained by our code are in good agreement with the analytical solutions for both para-sinuous and para-varicose modes, which are shown in Fig. 2.
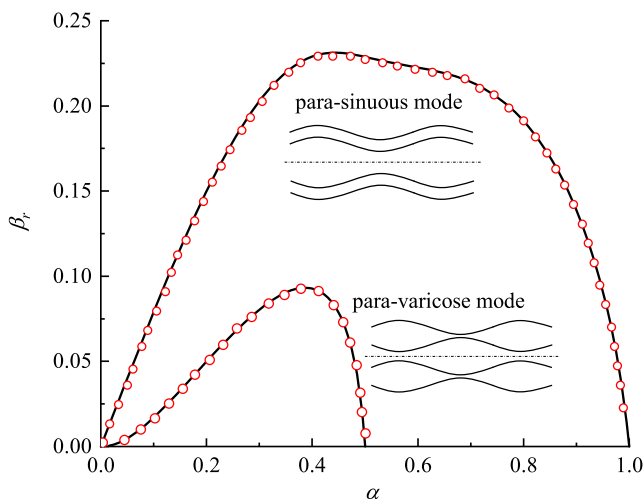
FIG. 2. Validation of the present code (black solid lines) compared with that in the work of Chauhan *et al.*[12] (red empty circles).

We consider the water–oil–gas system, which is commonly used in compound droplet production. It is assumed that the diameter of the coaxial jet is of the order of micrometers. The characteristic velocity is ~1 m/s. Considering the physical properties of fluids used here, we choose the following parameters as the reference state:

$$Re = 1, We = 2, Pe = 500, Ma = 150, T_{13} = 1.2,$$

$$\kappa_1 = 0.5, \kappa_2 = 7, \bar{U}_1 = 1.1, \sigma_{12} = 2, \gamma_{12} = 1,$$

$$C_{p12} = 2.7867, C_{p32} = 0.6693, k_{12} = 3.8735, k_{32} = 0.1427,$$

$$\mu_{12} = 0.0235, \mu_{32} = 0.0004, \rho_{12} = 1.0032, \rho_{32} = 0.0012.$$

Such dimensionless parameters are fixed to the reference values in the following discussion unless further stated.

A. Effect of the temperature difference on jet instability

The temperature ratio T_{13} reflects the difference between temperatures of inner fluids and surrounding fluids. We can describe coaxial jets at $T_{13} > 1$ as hot coaxial jets and those at $T_{13} < 1$ as cold coaxial jets correspondingly. The influence of the temperature ratio on the para-sinuous mode and the para-varicose mode is shown in Fig. 3(a). For both of them, the coaxial jet is more unstable as the temperature ratio decreases. The mechanism behind this behavior will be revealed by the energy budget below. The variation of the temperature ratio has no apparent effect on the wavenumber corresponding to the maximum disturbance growth rate of the para-sinuous mode, which is equivalent to 1.05. It shows that the disturbance wave component whose wavelength approximately equals the circumference of the outer fluid is the dominant one in the para-sinuous mode. The most unstable wavelength of the para-varicose mode is about twice that of the para-sinuous mode. The range of the unstable axial wavenumber slightly decreases with the increase in T_{13} for the para-sinuous mode. Meanwhile, it is apparently shrunk as the temperature of inner fluids rises for the para-varicose mode. Figure 3(b) illustrates the effect of the temperature ratio on the growth rates of the helical mode whose azimuthal wavenumber $n = 1$. It shows that the helical mode is more stable than the para-sinuous mode and is of the same order of the para-varicose mode. The disturbance growth rate is reduced when the temperature ratio is close to 1 for both hot and cold coaxial jets. However, the growth rate of the helical mode with an infinitely long-wave perturbation is non-zero and bigger than that of the para-sinuous mode, which is similar to the phenomenon found in coaxial jets under a radial electric field.[35] It means that the helical mode will dominate the flow if there is an infinitely long-wave perturbation. Those coaxial jets whose azimuthal wavenumbers are larger than 1 remain stable all the time, so we do not show them in the figure. Note that the para-sinuous mode, compared with the para-varicose and helical modes, plays a dominant role in the instability of coaxial jets under the radial thermal field, so we mainly focus on the behavior of it.

As mentioned above, to better understand the effect of the thermal field to the instability of coaxial jets, we balance the energy budget. Figure 4 illustrates the energy budget of five thermal-related terms vs the wavenumber. In the short wavelength region, these
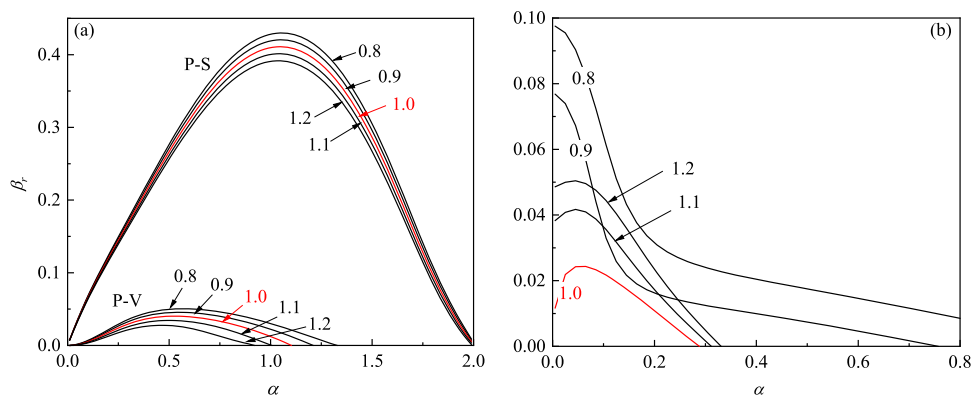
FIG. 3. The effect of the temperature ratio T_{13} on the growth rates of (a) the para-sinuous mode (P–S), the para-varicose mode (P–V), and (b) the helical mode.
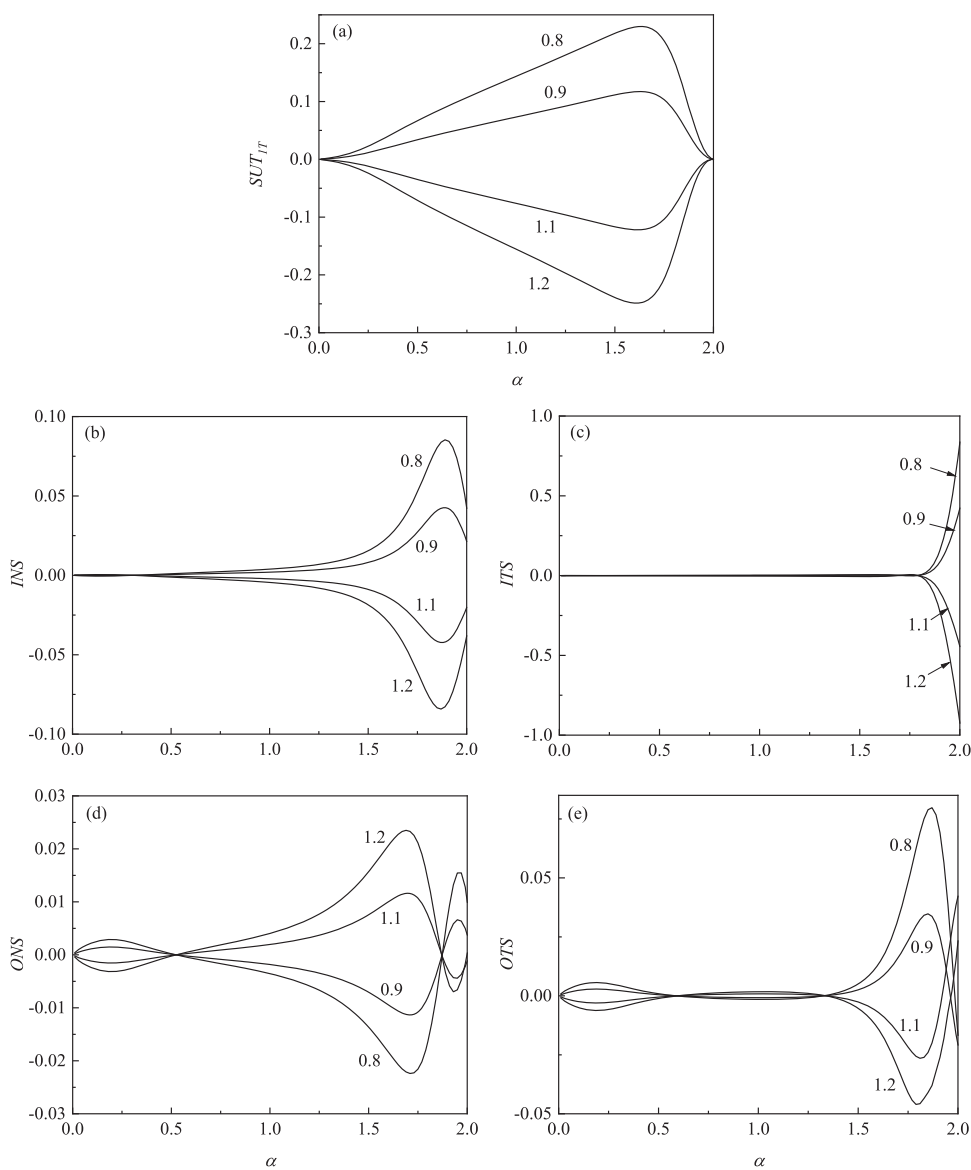

FIG. 4. Energy budget of thermal-related terms as a function of wavenumber for the para-sinuous mode at different temperature ratios T_{13} (from 0.8 to 1.2). (a) SUT_{1T}, (b) INS, (c) ITS, (d) ONS, and (e) OTS.

terms are more profound than those in the long wavelength region, which means the thermal-capillary instability and the Marangoni instability easily exist with the short-wave perturbation. In the long wavelength region, SUT_{1T} far outweighs the other four terms. When α reaches the most unstable wavenumber, the values of SUT_{1T} are much larger than those of other four terms, which means SUT_{1T}, compared with other thermal-related terms, is the dominant factor. It contributes to the jet instability if $T_{13} < 1$, and its effect is more significant with the decrease in T_{13}. However, it turns to stabilize the coaxial jet when $T_{13} > 1$, and its stabilized effect is enhanced by increasing the temperature of the inner fluid. INS, which is shown in Fig. 4(b), has a similar effect on jet instability with SUT_{1T}, except that INS tends to be more acute in the short-wavelength region than that in the long-wavelength region. As for ITS shown in Fig. 4(c), it has no influence on the jet instability until near the cut-off wavenumber whose wavelength is quite small and it contributes to the instability of cold coaxial jets and suppresses the instability of hot coaxial jets. When we consider the thermal stresses on the outer surface, it is more sophisticated. For Fig. 4(d), there are two critical wavenumbers near $\alpha = 0.5$ and $\alpha = 1.8$. When the wavenumber lies in the region between these two critical wavenumbers, ONS contributes to the growth of an unstable wave for hot coaxial jets and weakens it for cold coaxial jets. However, its effect on the jet instability is opposite in the remaining unstable wavenumber region. As for the effect of OTS, we can also observe two critical wavenumbers around $\alpha = 0.6$ and $\alpha = 1.3$, which is shown in Fig. 4(e). It has different impacts on the jet instability at different wavelength regions. When OTS is positive, it means that the Marangoni stress at the outer surface contributes to the jet instability. OTS tends to suppress the growth of the unstable disturbance when its value is negative.

B. Effect of the Marangoni flow on jet instability

The increase in Ma leads to a stronger Marangoni flow by a larger surface tension gradient than that of relatively low Ma. When $T_{13} > 1$, the jet instability is suppressed by increasing Ma for the para-sinuous mode shown in Fig. 5(a). It elucidates that the Marangoni flow will weaken the jet instability for hot coaxial jets. Changing Ma has little influence on the most unstable wavenumber, which is also equivalent to the circumference of the coaxial jet approximately. The cut-off wavenumber slightly decreases as Ma increases, which means that the range of the unstable wave is shrunk.
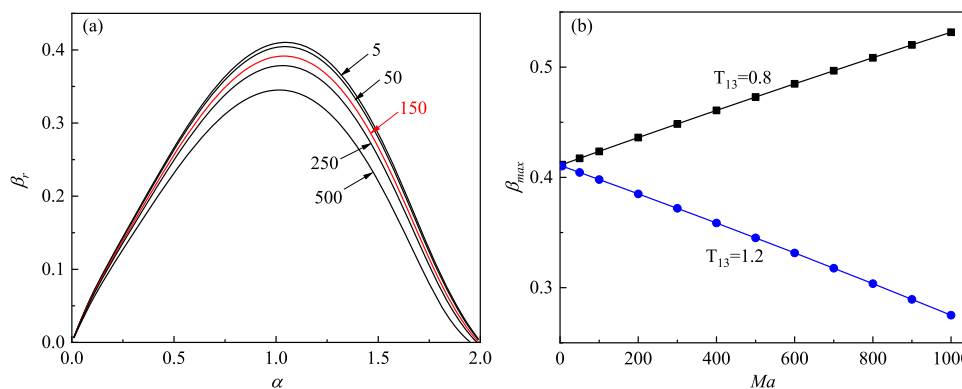
TABLE II. Energy budget of different Marangoni numbers at the most unstable disturbance wavenumber with $T_{13} = 0.8$ or $T_{13} = 1.2$.

T_{13}	Ma	α_{max}	SUT_{1T}	INS	ITS	ONS	OTS
0.8	50	1.05	0.0516	0.0015	0.0008	−0.0014	−0.0005
0.8	150	1.05	0.1509	0.0043	0.0022	−0.0040	−0.0015
0.8	300	1.06	0.2935	0.0083	0.0042	−0.0078	−0.0027
1.2	50	1.04	−0.0525	−0.0015	−0.0008	0.0014	0.0006
1.2	150	1.04	−0.1620	−0.0048	−0.0026	0.0045	0.0017
1.2	300	1.03	−0.3353	−0.0102	−0.0058	0.0094	0.0038

As shown in Fig. 5(b), the maximum disturbance growth rate monotonically declined with Ma linearly when $T_{13} > 1$, while it monotonically increased with Ma linearly when $T_{13} < 1$, which represents the dramatic difference between hot and cold coaxial jets. Thus, we can obtain more tiny compound droplets in cold coaxial jets with large Marangoni numbers than those in hot coaxial jets.

With the view of the energy budget shown in Table II, we can investigate the variation of thermal energy resources with different Ma for hot and cold coaxial jets. When $T_{13} = 0.8$, SUT_{1T}, INS, and ITS are positive factors to the jet instability, while ONS and OTS are negative ones. Their effects are all enhanced with increasing Ma. It illustrates that both thermal-capillary and Marangoni stresses at the inner interface contribute to the jet instability in cold coaxial jets, while these stresses at the outer surface tend to make the coaxial jets more stable. Meanwhile, SUT_{1T} is still the dominant factor among these terms caused by the thermal field, which shows that the increase in Ma will promote the jet breakup by enhancing capillary instability. However, as for $T_{13} = 1.2$, the terms SUT_T, INS, and ITS are all negative in hot coaxial jets, so they all suppress the jet instability. Their effects on the jet instability are strengthened by increasing Ma. The effects of ONS and OTS on the jet instability are still opposite to the other three terms, i.e., they make the coaxial jets more unstable. Increasing Ma also promotes their effects on the jet instability.

Increasing the ratio of temperature coefficients of the inner interfacial tension to the outer surface tension leads to a stronger Marangoni flow at the inner interface. Figure 6 shows the effect of
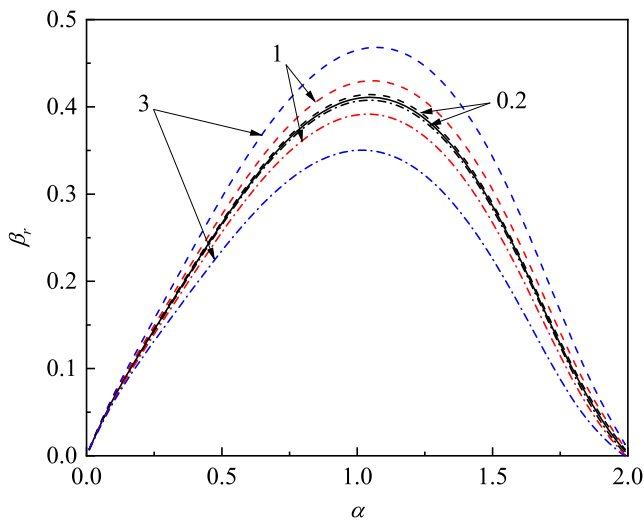

FIG. 5. The effect of the Marangoni number on jet instability for the para-sinuous mode. (a) The disturbance growth rates at $T_{13} = 1.2$ and (b) the maximum disturbance growth rates at $T_{13} = 0.8$ and $T_{13} = 1.2$, respectively.

FIG. 6. The effect of temperature coefficient ratio γ_{12} on the growth rate of the para-sinuous mode. Solid lines—T_{13} = 1.0, dashed lines—T_{13} = 0.8, and dashed-dotted lines—T_{13} = 1.2. Black—γ_{12} = 0.1, red—γ_{12} = 1, and blue—γ_{12} = 3.

TABLE III. Energy budget of different Péclet numbers at the most unstable disturbance wavenumber with T_{13} = 0.8 or T_{13} = 1.2.

T_{13}	Pe	α_{max}	SUT_{1T}	INS	ITS	ONS	OTS
0.8	150	1.07	0.4712	0.0249	0.0123	−0.0212	−0.0065
0.8	500	1.07	0.1538	0.0045	0.0023	−0.0042	−0.0015
0.8	1000	1.05	0.0769	0.0016	0.0008	−0.0015	−0.0006
1.2	150	1.01	−0.5827	−0.0339	−0.0208	0.0277	0.0123
1.2	500	1.04	−0.1620	−0.0048	−0.0026	0.0045	0.0017
1.2	1000	1.04	−0.0793	−0.0016	−0.0009	0.0016	0.0006

γ_{12} (differentiated by colors) on the jet instability with three different temperature ratios T_{13} = 0.8, 1, 1.2 (differentiated by line styles). Note that γ_{12} has no effect on the jet instability when T_{13} = 1, so three lines with different γ_{12} coincide to only one line, which is illustrated by black here. According to Fig. 6, the Marangoni flow at the inner interface will suppress the jet instability at T_{13} = 1.2. The mechanism of this phenomenon is that the thermal stress will be strengthened by increasing the relative temperature coefficient of the inner interfacial tension, which leads to a stronger Marangoni flow. According to the results obtained above, this stronger Marangoni flow makes hot coaxial jets more stable. On the contrary, we can learn from the dashed lines that the Marangoni flow enhances the jet instability when $T_{13} < 1$.

C. Effect of the heat transfer on jet instability

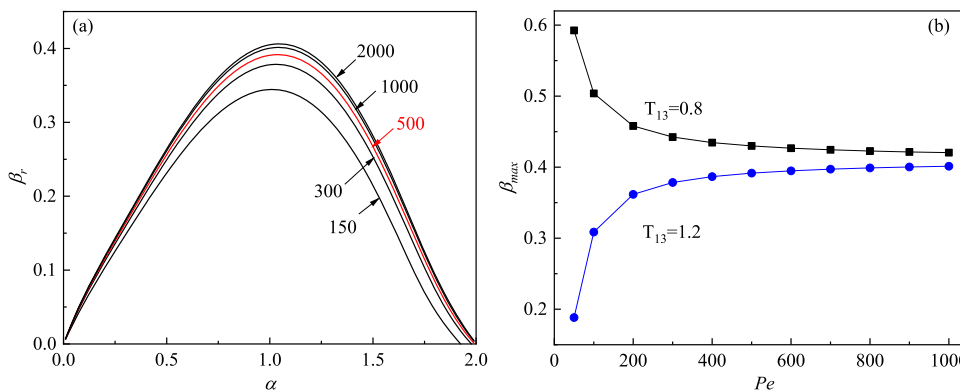Figure 7(a) illustrates the growth rates of the para-sinuous mode with different Pe in the hot coaxial jet cases. It can be seen that the coaxial jet is more unstable when Pe increases. It means that the heat transfer will suppress the jet instability when $T_{13} > 1$. The Péclet number has a slight influence on the most unstable wavenumber in the para-sinuous mode. The region of the unstable wavenumber expanded with the increase in Pe. Figure 7(b) illustrates the relation of the maximum growth rate to the Péclet number when T_{13} = 0.8 and T_{13} = 1.2. It shows that the instability of the hot coaxial jet is promoted as Pe increases until it reaches its saturation. However, for cold coaxial jets, the maximum growth rate keeps reducing until Pe is too large. It is opposite for hot jet cases.

When T_{13} = 0.8 shown in Table III, SUT_{1T}, INS, and ITS are positive, which means that they contribute to the jet instability. Their values increase as Pe declines. It means that their effects are strengthened when the heat transfer becomes stronger. The terms ONS and OTS still have opposite effects with others. Compared with their values, the term SUT_{1T} still keeps dominant in all cases and is more significant than other thermal-related terms. Considering the hot coaxial jets with T_{13} = 1.2, SUT_{1T}, INS, and ITS are negative factors to the jet instability, while ONS and OTS contribute to it. Their effects on jet instability are also enhanced with the stronger heat transfer effect. Hence, the heat transfer always tends to enhance the effects of the thermal field on the jet instability.

The thermal conductivity measures the ability of a substance to conduct heat. Heat transfer occurs at a higher rate in fluids with a high thermal conductivity than in those with a low thermal conductivity and points from a high temperature to low temperature. In Figs. 8(a) and 8(c), the overlap of lines with the same style
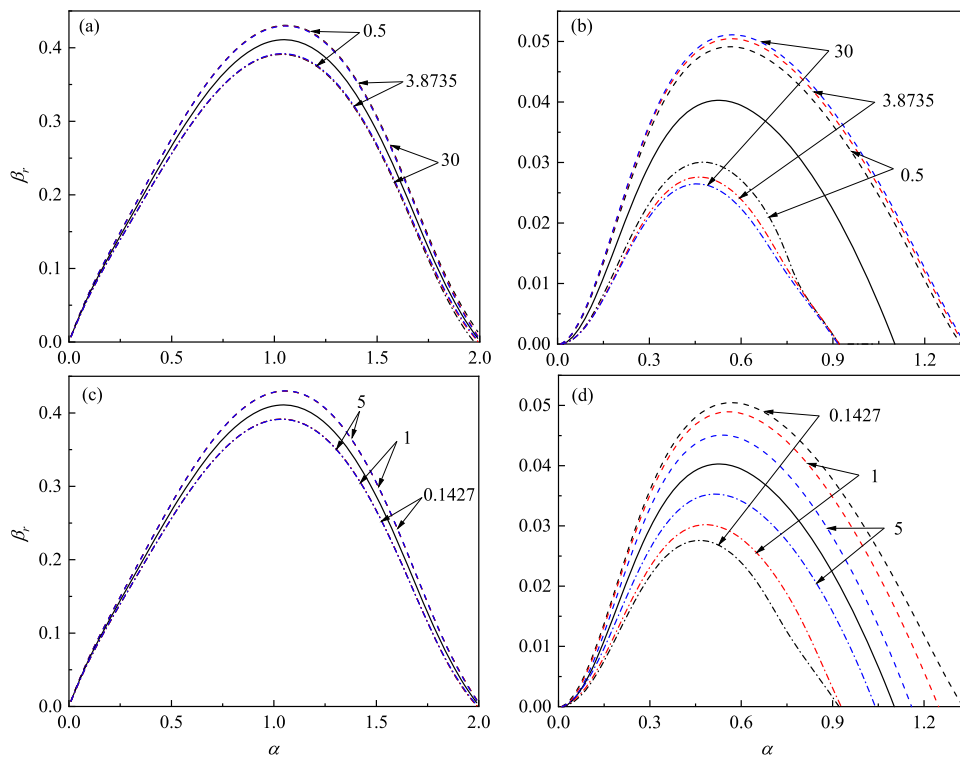

FIG. 7. The effect of the Péclet number on the jet instability of the para-sinuous mode. (a) The disturbance growth rates at T_{13} = 1.2 and (b) the maximum disturbance growth rates at T_{13} = 0.8 and T_{13} = 1.2, respectively.

FIG. 8. The effect of the thermal conductivity k_{12} on the disturbance growth rate of (a) the para-sinuous mode and (b) the para-varicose mode. The effect of the thermal conductivity k_{32} on the disturbance growth rate of (c) the para-sinuous mode and (d) the para-varicose mode. Solid lines—$T_{13} = 1$, dashed lines—$T_{13} = 0.8$, and dashed-dotted lines—$T_{13} = 1.2$.

illustrates that changing thermal conductivity of either inner fluids or surrounding fluids has no apparent influence on the jet instability for the para-sinuous mode. As shown in Fig. 8(b), the jet instability is promoted with the increase in k_{12} for the para-varicose mode at $T_{13} = 0.8$. The underlying mechanism of this tendency is that the heat received by the inner fluid from the outer fluid is easier to be transferred from the inner interface to the axis region in the high thermal conductivity than that in the low thermal conductivity. Therefore, the temperature of the inner interface is higher in low k_{12} than in high k_{12}. Because of the contribution of the inner interfacial tension, the jet instability is enhanced by increasing k_{12} at $T_{13} < 1$. As for the hot coaxial jets, the heat transfer direction is adverse to the cold coaxial jets. Therefore, the jet instability is suppressed with high k_{12} when $T_{13} > 1$, which is opposite to the cases at $T_{13} < 1$. As shown in Fig. 8(d), the jet instability is promoted as the increase in k_{32} for the para-varicose mode at $T_{13} = 1.2$. In these cases, the heat is easier to be transferred to the ambient in high k_{32} than in low k_{32}. As a consequence, the temperature of the outer surface decreases as k_{32} increases, which leads to the promotion of the jet instability. For coaxial jets at $T_{13} < 1$, the influence of k_{32} on the jet instability is opposite to the cases at $T_{13} > 1$ because of the different heat transfer direction.

D. Effect of the specific heat capacity on jet instability

Specific heat capacity of fluids measures the heat required to raise one degree of the unit mass. As a result, a higher specific heat capacity means that its temperature is more difficult to change relatively. As shown in Fig. 9(a), the variation of C_{p12} has no influence on the para-sinuous mode. For the para-varicose mode shown in Fig. 9(b), the difference of C_{p12} has apparent influences on the jet instability. When the inner fluid is hotter than the surrounding fluid, the jet instability is enhanced by reducing the inner specific heat capacity. In this case, the thermal energy transfers from inner fluids to surrounding fluids. When the inner specific heat capacity is reduced, the loss of temperature of inner fluids will increase accordingly. This means that the surface tension is higher for the relatively smaller inner specific heat capacity, which enhances the jet instability. Contrarily, when we consider the cold coaxial jets, i.e., the temperature ratio $T_{13} = 0.8 < 1$, the inner fluid will obtain heat transferred by the outer fluid, which causes an increase in the temperature of inner fluids. Then, the lower the specific heat capacity of inner fluids, the higher the temperature increase in them. Hence, the corresponding surface tension is relatively lower, which suppresses the jet instability.

As for the C_{p32} shown in Fig. 9(c), it also has no influence on the jet instability in the para-sinuous mode, which is similar to the effect of C_{p12}. The para-varicose mode is more sensitive to the variation of C_{p32} than the para-sinuous mode, as shown in Fig. 9(d). The jet instability is enhanced with the increase in the specific heat capacity of the surrounding fluid when there are hot coaxial jets. In these cases, the surrounding fluid will receive heat from outer fluids, which causes the positive temperature fluctuation at the outer surface. When the specific heat capacity ratio C_{p32} increases, the positive temperature fluctuation will accordingly reduce. Then, the outer surface tension is relatively higher for high C_{p32} than that of small C_{p32}, which makes the coaxial jet more unstable. When the surrounding fluid is hotter than the inner fluid, the jet instability
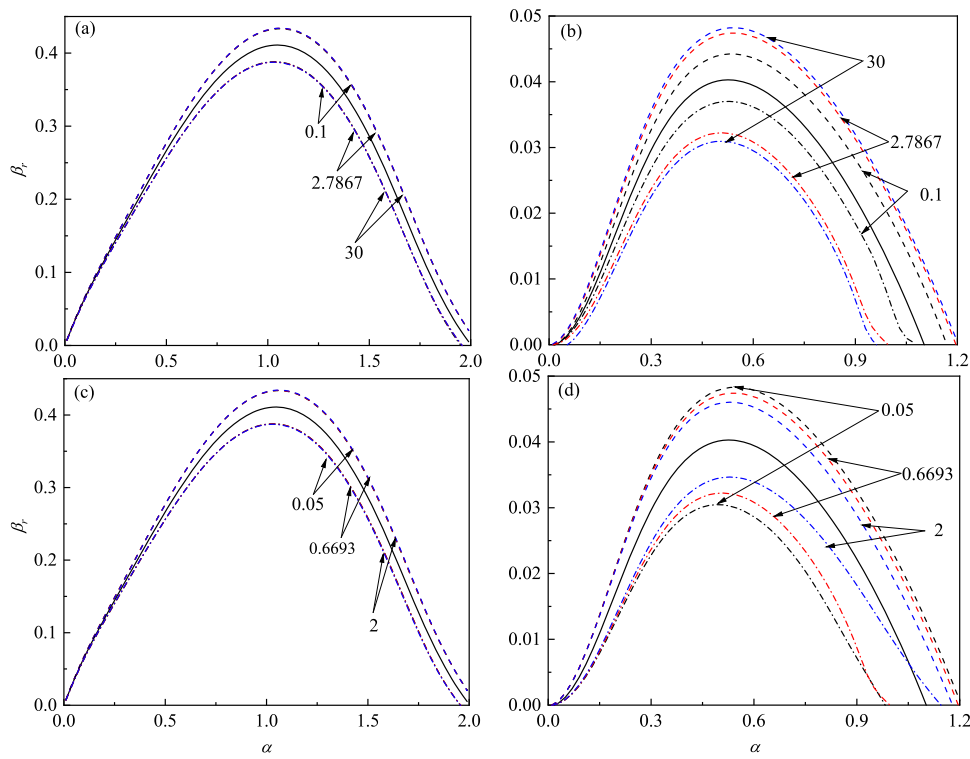
FIG. 9. The effect of the specific heat capacity ratio C_{p12} on the disturbance growth rate of (a) the para-sinuous mode and (b) the para-varicose mode. The effect of the specific heat capacity ratio C_{p32} on the disturbance growth rate of (c) the para-sinuous mode and (d) the para-varicose mode. Solid lines—T_{13} = 1, dashed lines—T_{13} = 0.8, and dashed-dotted lines—T_{13} = 1.2.

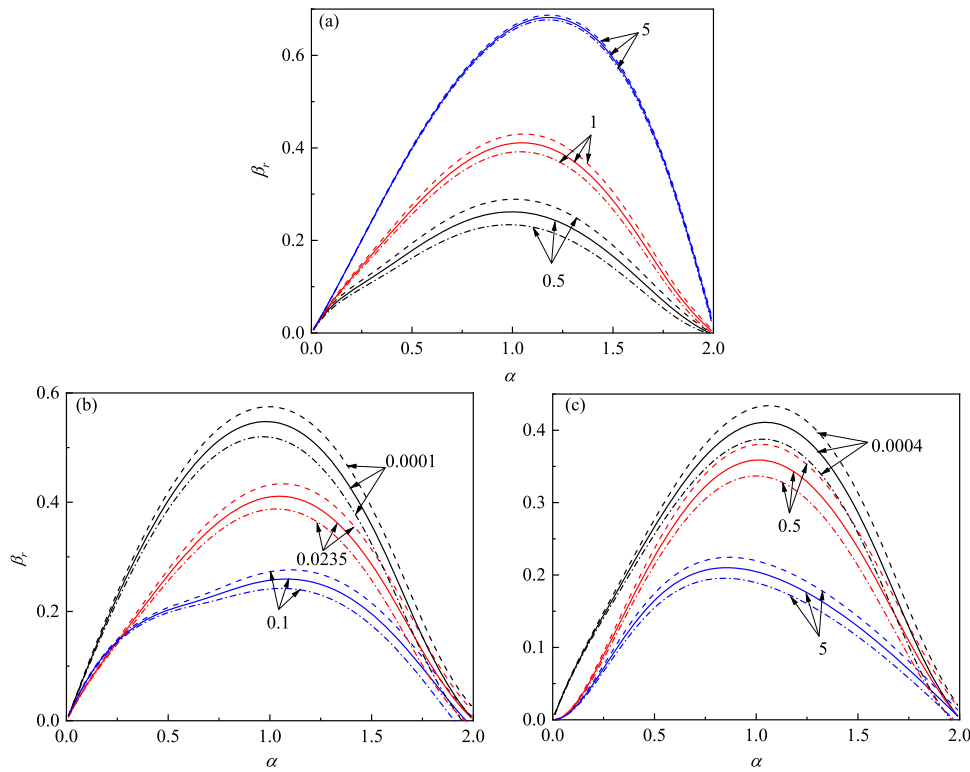**FIG. 10**. The effect of viscosity on the disturbance growth rate of the para-sinuous mode. Effects of (a) the Reynolds number, (b) the viscosity ratio μ_{12}, and (c) the viscosity ratio μ_{32}. Solid lines—T_{13} = 1, dashed lines—T_{13} = 0.8, and dashed-dotted lines—T_{13} = 1.2.

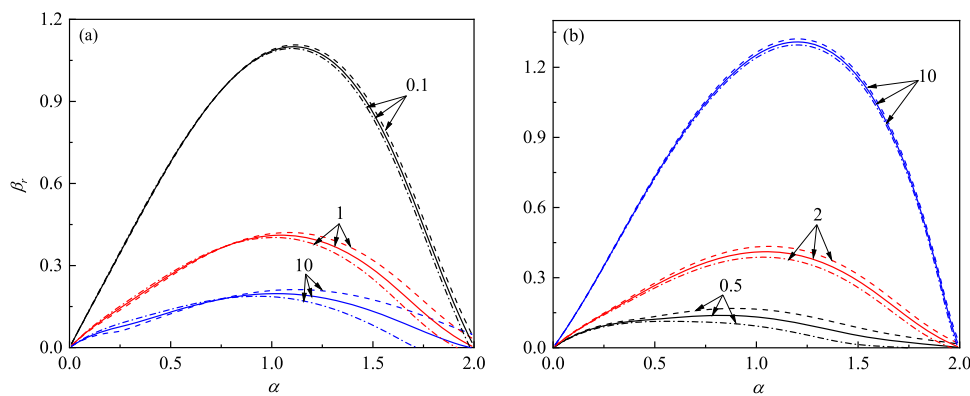FIG. 11. The effect of surface tension on the disturbance grow rate of the para-sinuous mode. Effects of (a) the Weber number and (b) the ratio of the inner interfacial tension to the outer surface tension. Solid lines—T_{13} = 1, dashed lines—T_{13} = 0.8, and dashed-dotted lines—T_{13} = 1.2.

is enhanced with the decrease in C_{p32}, which also results from the relative high outer surface tension caused by the high heat loss of surrounding fluids with low C_{p32}.

E. Effects of viscosity and surface tension on jet instability

The jet instability is enhanced when the value of Re increases, as indicated in Fig. 10(a). The thermal effect has an obvious influence on the jet instability with low Re, but the difference among them is reduced with the increase in Re. It illustrates that the effect of thermal field is suppressed when the viscosity of three fluids increases proportionally. Figures 10(b) and 10(c) illustrate the effects of μ_{12} and μ_{32} on the para-sinuous mode, respectively. The disturbance growth rate is reduced by increasing the viscosity of either the inner fluid or the surrounding fluid. Note that changing the viscosity of either inner or surrounding fluids shows no effect on the unstable wavelength region.

As shown in Fig. 11(a), the maximum growth rate apparently increases with a decrease in the Weber number (We), which shows that the outer surface tension promotes the jet instability. When We is small, the influence of the temperature ratio on the jet instability tends to vanish on both the growth rate and unstable wavelength region, which shows that the effect of surface tension is dominant than that of the thermal effect. Moreover, the outer surface tension has a two-fold effect. In the relative short-wavelength region with the most unstable wave standing, the outer surface tension promotes the disturbance growth rate. However, it tends to suppress the jet instability when the wavenumber is smaller than a critical value. As shown in Fig. 11(b), increasing inner surface tension will also promote the jet instability obviously but has no apparent influence on the unstable wavelength region. Similar to the change in the Weber number, the difference among them in high σ_{12}, e.g., σ_{12} = 10, also tends to vanish because of the dominance of inner interfacial tension.

IV. CONCLUSION

A temporal linear instability is studied on the coaxial jets with axisymmetric and non-axisymmetric disturbances under a radial thermal field. Three unstable modes are identified, including the para-sinuous mode, the para-varicose mode, and the helical mode.

The effects of main controllable parameters on the jet instability are analyzed in combination of the energy budget method. With the decrease in temperature ratio T_{13}, the instability of coaxial jets is promoted. The difference between the interfacial tension that changes with T_{13} and its referenced value at T_{13} = 1, marked as SUT_{1T}, is the main thermal-related factor contributing to the jet instability. It enhances the jet instability at $T_{13} < 1$ but turns to suppress it at $T_{13} > 1$. Considering the wavenumber corresponding to the maximum growth rate, the energy budget shows that the rates of work done by the thermal-capillary stress on the inner interface (INS) and Marangoni stress on the inner interface (ITS) have the same effects with SUT_{1T}, while the rates of work done by the thermal-capillary stress on the outer surface (ONS) and the Marangoni stress on the outer surface (OTS) are opposite with all of them. As for hot coaxial jets, the Marangoni flow will suppress the jet instability and the maximum growth rate decreases linearly with the Marangoni number. However, its influence on jet instability will be the opposite for cold coaxial jets, and the maximum growth rate increases linearly with the Marangoni number. Increasing the temperature coefficient of inner interfacial tension will promote the jet instability with $T_{13} < 1$ and weaken it with $T_{13} > 1$. Considering the effect of heat transfer, the jet instability will be suppressed by it for hot coaxial jets, and the maximum growth rate will increase with the Péclet number until it reaches its saturation. Similarly, the behavior of cold coaxial jets is opposite to those of hot coaxial jets. Changing the thermal conductivity ratio k_{12} and k_{32} have no apparent influence on the jet instability for the para-sinuous mode. However, the para-varicose mode is more sensitive to the variation of the thermal conductivity ratio. Decreasing k_{12} or increasing k_{32} has a destabilized effect on the jet instability at $T_{13} > 1$ in the para-varicose mode. Their effect is opposite at $T_{13} < 1$ because of different heat conductivity directions. The variation of specific heat capacity of either inner or surrounding fluids has no influence on the jet instability of the para-sinuous mode. However, decreasing C_{p12} or increasing C_{p32} tends to promote the jet instability for hot coaxial jets and suppress the jet instability for cold coaxial jets in the para-varicose mode. Increasing the viscosity of any fluid will suppress the jet instability. When the Reynolds number is large, the effect of a thermal field tends to be suppressed. The inner interfacial tension and the outer surface tension are both positive factors to the breakup of coaxial jets. When the inner interfacial tension and the outer surface tension become large, the influence of the temperature ratio on the jet instability

tends to vanish on both disturbance growth rates and the unstable wavelength region. The results presented here would provide significant guidance for various practical applications in understanding the breakup behaviors of thermal coaxial jets into droplets.

ACKNOWLEDGMENTS

APPENDIX A: THE EXPRESSIONS OF MATRICES A, B

Considering the complexity of the original matrices A and B, we do not expand them with the Chebyshev polynomial in this appendix, i.e., $X = (\hat{u}_1, \hat{v}_1, \hat{w}_1, \hat{p}_1, \hat{T}_1, \hat{u}_2, \hat{v}_2, \hat{w}_2, \hat{p}_2, \hat{T}_2, \hat{u}_3, \hat{v}_3, \hat{w}_3, \hat{p}_3, \hat{T}_3)^T$. Therefore, two corresponding matrices are

$$
A = \begin{bmatrix} A_1 & & \\ & A_2 & \\ & & A_3 \end{bmatrix},
$$

$$
A_1 = \begin{bmatrix}
a_1 & -\dfrac{dU_1}{dr} & 0 & -\dfrac{i\alpha}{\rho_{12}} & 0 \\
0 & a_2 & -\dfrac{1}{Re_1}\dfrac{2in}{r^2} & -\left(\dfrac{1}{\rho_{12}}\right)\dfrac{d}{dr} & 0 \\
0 & \dfrac{1}{Re_1}\dfrac{2in}{r^2} & a_3 & -\left(\dfrac{1}{\rho_{12}}\right)\dfrac{in}{r} & 0 \\
i\alpha & \dfrac{d}{dr}+\dfrac{1}{r} & \dfrac{in}{r} & 0 & 0 \\
0 & 0 & 0 & 0 & a_5
\end{bmatrix},
$$

$$
A_2 = \begin{bmatrix}
a_6 & -\dfrac{dU_2}{dr} & 0 & -i\alpha & 0 \\
0 & a_7 & -\dfrac{1}{Re}\dfrac{2in}{r^2} & -\dfrac{d}{dr} & 0 \\
0 & \dfrac{1}{Re}\dfrac{2in}{r^2} & a_8 & -\dfrac{in}{r} & 0 \\
i\alpha & \dfrac{d}{dr}+\dfrac{1}{r} & \dfrac{in}{r} & 0 & 0 \\
0 & -\dfrac{Pe(1-T_{13})}{1-\kappa_1} & 0 & 0 & a_{10}
\end{bmatrix},
$$

$$
A_3 = \begin{bmatrix}
a_{11} & -\dfrac{dU_3}{dr} & 0 & -\dfrac{i\alpha}{\rho_{32}} & 0 \\
0 & a_{12} & -\dfrac{1}{Re_3}\dfrac{2in}{r^2} & -\left(\dfrac{1}{\rho_{32}}\right)\dfrac{d}{dr} & 0 \\
0 & \dfrac{1}{Re_3}\dfrac{2in}{r^2} & a_{13} & -\left(\dfrac{1}{\rho_{32}}\right)\dfrac{in}{r} & 0 \\
i\alpha & \dfrac{d}{dr}+\dfrac{1}{r} & \dfrac{in}{r} & 0 & 0 \\
0 & 0 & 0 & 0 & a_{15}
\end{bmatrix},
$$

$$
B = \begin{bmatrix} B_1 & & \\ & B_2 & \\ & & B_3 \end{bmatrix},
$$

$$
B_1 = \begin{bmatrix}
1 & 0 & 0 & 0 & 0 \\
0 & 1 & 0 & 0 & 0 \\
0 & 0 & 1 & 0 & 0 \\
0 & 0 & 0 & 0 & 0 \\
0 & 0 & 0 & 0 & \dfrac{Pe\rho_{12}C_{p12}}{k_{12}}
\end{bmatrix},
$$

$$
B_2 = \begin{bmatrix}
1 & 0 & 0 & 0 & 0 \\
0 & 1 & 0 & 0 & 0 \\
0 & 0 & 1 & 0 & 0 \\
0 & 0 & 0 & 0 & 0 \\
0 & 0 & 0 & 0 & Pe
\end{bmatrix},
$$

$$
B_3 = \begin{bmatrix}
1 & 0 & 0 & 0 & 0 \\
0 & 1 & 0 & 0 & 0 \\
0 & 0 & 1 & 0 & 0 \\
0 & 0 & 0 & 0 & 0 \\
0 & 0 & 0 & 0 & \dfrac{Pe\rho_{32}C_{p32}}{k_{32}}
\end{bmatrix},
$$

where

$$
a_1 = \frac{1}{Re_1}\left[\frac{d^2}{dr^2}+\frac{1}{r}\frac{d}{dr}-\left(\alpha^2+\frac{n^2}{r^2}+i\alpha Re_1 U_1\right)\right],
$$

$$
a_2 = a_3 = \frac{1}{Re_1}\left[\frac{d^2}{dr^2}+\frac{1}{r}\frac{d}{dr}-\left(\alpha^2+\frac{n^2+1}{r^2}+i\alpha Re_1 U_1\right)\right],
$$

$$
a_5 = \frac{d^2}{dr^2}+\frac{1}{r}\frac{d}{dr}-\left(\alpha^2+\frac{n^2}{r^2}+\frac{i\alpha U_1 Pe\rho_{12}C_{p12}}{k_{12}}\right),
$$

$$
a_6 = \frac{1}{Re}\left[\frac{d^2}{dr^2}+\frac{1}{r}\frac{d}{dr}-\left(\alpha^2+\frac{n^2}{r^2}+i\alpha Re U_2\right)\right],
$$

$$
a_7 = a_8 = \frac{1}{Re}\left[\frac{d^2}{dr^2}+\frac{1}{r}\frac{d}{dr}-\left(\alpha^2+\frac{n^2+1}{r^2}+i\alpha Re U_2\right)\right],
$$

$$
a_{10} = \frac{d^2}{dr^2}+\frac{1}{r}\frac{d}{dr}-\left(\alpha^2+\frac{n^2}{r^2}+i\alpha U_2 Pe\right),
$$

$$
a_{11} = \frac{1}{Re_3}\left[\frac{d^2}{dr^2}+\frac{1}{r}\frac{d}{dr}-\left(\alpha^2+\frac{n^2}{r^2}+i\alpha Re_3 U_3\right)\right],
$$

$$
a_{12} = a_{13} = \frac{1}{Re_3}\left[\frac{d^2}{dr^2}+\frac{1}{r}\frac{d}{dr}-\left(\alpha^2+\frac{n^2+1}{r^2}+i\alpha Re_3 U_3\right)\right],
$$

$$
a_{15} = \frac{d^2}{dr^2}+\frac{1}{r}\frac{d}{dr}-\left(\alpha^2+\frac{n^2}{r^2}+\frac{i\alpha U_3 Pe\rho_{32}C_{p32}}{k_{32}}\right).
$$

APPENDIX B: THE EXPRESSIONS INVOLVED IN THE ENERGY BUDGET

For inner fluids,

$$KE_1 = \frac{2\pi}{T\lambda}\int_0^T\int_0^{\kappa_1}\int_0^{\lambda}\left(\frac{\partial}{\partial t}+U_1\frac{\partial}{\partial z}\right)\left(\frac{u_1^2+v_1^2}{2}\right)r\,dz\,dr\,dt,$$

$$REY_1 = -\frac{2\pi}{T\lambda}\int_0^T\int_0^{\kappa_1}\int_0^{\lambda}v_1 u_1\frac{\partial U_1}{\partial r}r\,dz\,dr\,dt,$$

$$PRL_{1S} = -\frac{2\pi}{T\lambda S}\int_0^T\int_0^{\lambda}\left(v_1 p_2\right)_{r=\kappa_1}\kappa_1\,dz\,dt,$$

$$NVL_{1S} = \frac{2\pi}{T\lambda SRe}\int_0^T\int_0^{\lambda}\left[2v_1\frac{\partial v_2}{\partial r}\right]_{r=\kappa_1}\kappa_1\,dz\,dt,$$

$$SUT_1 = \frac{2\pi}{T\lambda S}\int_0^T\int_0^{\lambda}\left[\frac{\sigma_{12}}{We}v_1\left(\frac{\partial^2}{\partial z^2}+\frac{1}{\kappa_1^2}\right)\eta_1\right]_{r=\kappa_1}\kappa_1\,dz\,dt,$$

$$SUT_{1T} = -\frac{2\pi}{T\lambda S}\int_0^T\int_0^{\lambda}\gamma_{12}\frac{Ma}{PeRe}(T_{13}-1)$$
$$\times\left[v_1\left(\frac{\partial^2}{\partial z^2}+\frac{1}{\kappa_1^2}\right)\eta_1\right]_{r=\kappa_1}\kappa_1\,dz\,dt,$$

$$PRL_{1R} = -\frac{2\pi}{T\lambda S}\int_0^T\int_0^{\kappa_1}\left[u_1 p_1\right]_{z=0}^{z=\lambda}r\,dr\,dt,$$

$$SHL_{1R} = \frac{2\pi}{T\lambda Re_1}\int_0^T\int_0^{\kappa_1}v_1\left[\frac{\partial u_1}{\partial r}+\frac{\partial v_1}{\partial z}\right]_{z=0}^{z=\lambda}r\,dr\,dt,$$

$$NVL_{1R} = \frac{2\pi}{T\lambda Re_1}\int_0^T\int_0^{\kappa_1}\left[2u_1\frac{\partial u_1}{\partial r}\right]_{z=0}^{z=\lambda}r\,dr\,dt,$$

$$SHB_1 = \frac{2\pi}{T\lambda Re_1}\int_0^T\int_0^{\lambda}u_1\eta_1\left(\frac{1}{N}\frac{d^2 U_2}{dr^2}-\frac{d^2 U_1}{dr^2}\right)_{r=\kappa_1}\kappa_1\,dz\,dt,$$

$$SHL_{1S} = \frac{2\pi}{T\lambda Re_1 N}\int_0^T\int_0^{\lambda}\left[u_1\left(\frac{\partial u_2}{\partial r}+\frac{\partial v_2}{\partial z}\right)\right]_{r=\kappa_1}\kappa_1\,dz\,dt,$$

$$DIS_1 = -\frac{2\pi}{T\lambda Re_1}\int_0^T\int_0^{\kappa_1}\int_0^{\lambda}\left[2\left(\frac{\partial v_1}{\partial r}\right)^2+2\left(\frac{\partial u_1}{\partial z}\right)^2+2\left(\frac{v_1}{r}\right)^2\right.$$
$$\left.+\left(\frac{\partial u_1}{\partial r}+\frac{\partial v_1}{\partial z}\right)^2\right]r\,dz\,dr\,dt,$$

$$INS = \frac{2\pi}{T\lambda S}\int_0^T\int_0^{\lambda}\gamma_{12}\frac{Ma}{PeRe}\left(v_1\frac{T_1}{\kappa_1}\right)_{r=\kappa_1}\kappa_1\,dz\,dt,$$

$$ITS = \frac{2\pi}{T\lambda N}\int_0^T\int_0^{\lambda}\left[\gamma_{12}\frac{Ma}{PeRe}\frac{\partial T_1}{\partial z}u_1\right]_{r=\kappa_1}\kappa_1\,dz\,dt.$$

For outer fluids,

$$KE_2 = \frac{2\pi}{T\lambda}\int_0^T\int_{\kappa_1}^{1}\int_0^{\lambda}\left(\frac{\partial}{\partial t}+U_2\frac{\partial}{\partial z}\right)\left(\frac{u_2^2+v_2^2}{2}\right)r\,dz\,dr\,dt,$$

$$REY_2 = -\frac{2\pi}{T\lambda}\int_0^T\int_{\kappa_1}^{1}\int_0^{\lambda}v_2 u_2\frac{dU_2}{dr}r\,dz\,dr\,dt,$$

$$PRG_2 = -\frac{2\pi}{T\lambda}\int_0^T\int_0^{\lambda}\left(v_2 p_3\right)_{r=1}\,dz\,dt,$$

$$NVG_2 = \frac{2\pi M}{T\lambda Re}\int_0^T\int_0^{\lambda}\left[2v_2\frac{\partial v_3}{\partial r}\right]_{r=1}\,dz\,dt,$$

$$SUT_2 = \frac{2\pi}{T\lambda}\int_0^T\int_0^{\lambda}\frac{1}{We}\left[v_2\left(\frac{\partial^2}{\partial z^2}+1\right)\eta_2\right]_{r=1}\,dz\,dt,$$

$$PRL_{2S} = \frac{2\pi}{T\lambda}\int_0^T\int_0^{\lambda}\left[v_2 p_2\right]_{r=\kappa_1}\kappa_1\,dz\,dt,$$

$$PRL_{2R} = -\frac{2\pi}{T\lambda}\int_0^T\int_{\kappa_1}^{1}\left[u_2 p_2\right]_{z=0}^{z=\lambda}r\,dr\,dt,$$

$$SHB_2 = \frac{2\pi}{T\lambda Re}\int_0^T\int_0^{\lambda}u_2\eta_2\left(M\frac{d^2 U_3}{dr^2}-\frac{d^2 U_2}{dr^2}\right)_{r=1}\,dz\,dt,$$

$$SHG_2 = \frac{2\pi}{T\lambda Re}\int_0^T\int_0^{\lambda}Mu_2\left(\frac{\partial u_3}{\partial r}+\frac{\partial v_3}{\partial z}\right)_{r=1}\,dz\,dt,$$

$$SHL_{2S} = -\frac{2\pi}{T\lambda Re}\int_0^T\int_0^{\lambda}\left[u_2\left(\frac{\partial u_2}{\partial r}+\frac{\partial v_2}{\partial z}\right)\right]_{r=\kappa_1}\kappa_1\,dz\,dt,$$

$$NVL_2 = \frac{2\pi}{T\lambda Re}\int_0^T\int_{\kappa_1}^{1}\left[2u_2\frac{\partial u_2}{\partial z}\right]_{z=0}^{z=\lambda}r\,dr\,dt,$$

$$SHL_{2R} = \frac{2\pi}{T\lambda Re}\int_0^T\int_{\kappa_1}^{1}\left[v_2\left(\frac{\partial u_2}{\partial r}+\frac{\partial v_2}{\partial z}\right)\right]_{z=0}^{z=\lambda}r\,dr\,dt,$$

$$DIS_2 = -\frac{2\pi}{T\lambda Re}\int_0^T\int_{\kappa_1}^{1}\int_0^{\lambda}\left[2\left(\frac{\partial v_2}{\partial r}\right)^2+2\left(\frac{\partial u_2}{\partial z}\right)^2+2\left(\frac{v_2}{r}\right)^2\right.$$
$$\left.+\left(\frac{\partial u_2}{\partial r}+\frac{\partial v_2}{\partial z}\right)^2\right]r\,dz\,dr\,dt,$$

$$ONS = -\frac{2\pi}{T\lambda}\int_0^T\int_0^{\lambda}\frac{Ma}{PeRe}(v_2 T_3)_{r=1}\,dz\,dt,$$

$$OTS = \frac{2\pi}{T\lambda}\int_0^T\int_0^{\lambda}\left[\frac{Ma}{PeRe}\frac{\partial T_3}{\partial z}u_2\right]_{r=1}\,dz\,dt.$$

DATA AVAILABILITY

The data that support the findings of this study are available from the corresponding author upon reasonable request.

REFERENCES

[1] O. A. Basaran, H. Gao, and P. P. Bhat, "Nonstandard inkjets," Annu. Rev. Fluid Mech. **45**, 85–113 (2013).

[2] E. J. Vega, A. M. Gañán-Calvo, J. M. Montanero, M. G. Cabezas, and M. A. Herrada, "A novel technique for producing metallic microjets and microdrops," Microfluid. Nanofluid. **14**, 101–111 (2013).

[3] J. J. Kaufman, G. Tao, S. Shabahang, E.-H. Banaei, D. S. Deng, X. Liang, S. G. Johnson, Y. Fink, and A. F. Abouraddy, "Structured spheres generated by an in-fibre fluid instability," Nature **487**, 463–467 (2012).

[4] G. Loke, W. Yan, T. Khudiyev, G. Noel, and Y. Fink, "Recent progress and perspectives of thermally drawn multimaterial fiber electronics," Adv. Mater. **32**, 1904911 (2020).

[5] G. Balestra, M. Gloor, and L. Kleiser, "Absolute and convective instabilities of heated coaxial jet flow," Phys. Fluids **27**, 054101 (2015).

[6] M. Gloor, S. Bühler, and L. Kleiser, "Transition to turbulence and noise radiation in heated coaxial jet flows," Phys. Fluids **28**, 044103 (2016).

[7] C. H. Hertz and B. Hermanrud, "A liquid compound jet," J. Fluid Mech. **131**, 271 (1983).

[8] A. Sanz and J. Meseguer, "One-dimensional linear analysis of the compound jet," J. Fluid Mech. **159**, 55–68 (1985).

[9] J. Meyer and D. Weihs, "Capillary instability of an annular liquid jet," J. Fluid Mech. **179**, 531 (1987).

[10] S. Radev and B. Tchavdarov, "Linear capillary instability of compound jets," Int. J. Multiphase Flow **14**, 67–79 (1988).

[11] J. Shen and X. Li, "Instability of an annular viscous liquid jet," Acta Mech. **114**, 167–183 (1996).

[12] A. Chauhan, C. Maldarelli, D. T. Papageorgiou, and D. S. Rumschitzki, "Temporal instability of compound threads and jets," J. Fluid Mech. **420**, 1–25 (2000).

[13] F. Chen, J.-Y. Tsaur, F. Durst, and S. K. Das, "On the axisymmetry of annular jet instabilities," J. Fluid Mech. **488**, 355–367 (2003).

[14] A.-C. Ruo, F. Chen, and M.-H. Chang, "Linear instability of compound jets with nonaxisymmetric disturbances," Phys. Fluids **21**, 012101 (2009).

[15] A. Segalini and A. Talamelli, "Experimental analysis of dominant instabilities in coaxial jets," Phys. Fluids **23**, 024103 (2011).

[16] M. F. Afzaal, J. Uddin, A. M. Alsharif, and M. Mohsin, "Temporal and spatial instability of a compound jet in a surrounding gas," Phys. Fluids **27**, 044106 (2015).

[17] M. F. Afzaal and J. Uddin, "Nonaxisymmetric disturbances in compound liquid jets falling under gravity," Phys. Rev. E **94**, 043114 (2016).

[18] H.-Y. Ye, L.-J. Yang, and Q.-F. Fu, "Instability of viscoelastic compound jets," Phys. Fluids **28**, 043101 (2016).

[19] Z. H. Chaudhury, "Heat transfer in a radial liquid jet," J. Fluid Mech. **20**, 501–511 (1964).

[20] A. E. Gill and P. G. Drazin, "Note on instability of compressible jets and wakes to long-wave disturbances," J. Fluid Mech. **22**, 415 (1965).

[21] J.-J. Xu and S. H. Davis, "Instability of capillary jets with thermocapillarity," J. Fluid Mech. **161**, 1–25 (1985).

[22] P. A. Monkewitz and K. D. Sohn, "Absolute instability in hot jets," AIAA J. **26**, 911–916 (1988).

[23] H. A. Dijkstra and P. H. Steen, "Thermocapillary stabilization of the capillary breakup of an annular film of liquid," J. Fluid Mech. **229**, 205–228 (1991).

[24] F. Mashayek and N. Ashgriz, "Nonlinear instability of liquid jets with thermocapillarity," J. Fluid Mech. **283**, 97–123 (1995).

[25] E. P. Furlani, "Temporal instability of viscous liquid microjets with spatially varying surface tension," J. Phys. A: Math. Theor. **38**, 263–276 (2005).

[26] D. Perrault-Joncas and S. A. Maslowe, "Linear stability of a compressible coaxial jet with continuous velocity and temperature profiles," Phys. Fluids **20**, 074102 (2008).

[27] L. Mohanta, F.-B. Cheung, and S. M. Bajorek, "Stability of coaxial jets confined in a tube with heat and mass transfer," Physica A **443**, 333–346 (2016).

[28] S. Mowlavi, I. Shukla, P.-T. Brun, and F. Gallaire, "Particle size selection in capillary instability of locally heated coaxial fiber," Phys. Rev. Fluids **4**, 064003 (2019).

[29] B. Jia, L. Xie, X. Cui, L. Yang, and Q. Fu, "Linear stability of confined coaxial jets in the presence of gas velocity oscillations with heat and mass transfer," Phys. Fluids **31**, 092101 (2019).

[30] S. Li, R. Yang, K. Mu, X. Luo, and T. Si, "Thermal effects on the instability of coaxial liquid jets in the core of a gas stream," Phys. Fluids **31**, 032106 (2019).

[31] M. Lappa, R. Savino, and R. Monti, "Three-dimensional numerical simulation of Marangoni instabilities in liquid bridges: Influence of geometrical aspect ratio," Int. J. Numer. Methods Fluids **36**, 53–90 (2001).

[32] P. Yecko, S. Zaleski, and J.-M. Fullana, "Viscous modes in two-phase mixing layers," Phys. Fluids **14**, 4115–4122 (2002).

[33] G. Li, X. Luo, T. Si, and R. X. Xu, "Temporal instability of coflowing liquid-gas jets under an electric field," Phys. Fluids **26**, 054101 (2014).

[34] S. P. Lin and J. N. Chen, "Role played by the interfacial shear in the instability mechanism of a viscous liquid jet surrounded by a viscous gas in a pipe," J. Fluid Mech. **376**, 37–51 (1998).

[35] F. Li, X.-Y. Yin, and X.-Z. Yin, "Axisymmetric and non-axisymmetric instability of an electrified viscous coaxial jet," J. Fluid Mech. **632**, 199–225 (2009).

[36] J.-P. Matas, A. Delon, and A. Cartellier, "Shear instability of an axisymmetric air–water coaxial jet," J. Fluid Mech. **843**, 575–600 (2018).

[37] H. Ye, J. Peng, and L. Yang, "Instability of eccentric compound threads," Phys. Fluids **29**, 082110 (2017).